Electro-thermal heating element with a nickel-plated carbon fabric for the leading edge of a wing-shaped composite application

Jun-sung Lee[a,+], Hyeonseung Jo[b,+], Hyeon-seok Choe[a], Dae-sung Lee[a], Hojin Jeong[b], Hye-ree Lee[c], Jin-hwe Kweon[a], Hakjin Lee[b,]*, Rho Shin Myong[b,]*, and Youngwoo Nam[a,]*

[a]School of Mechanical and Aerospace Engineering, Gyeongsang National University
Composite Structures Laboratory
407-805, 501 Jinju-daero, Jinju, Gyeongnam 52828, Republic of Korea

[b]School of Mechanical and Aerospace Engineering, Gyeongsang National University
Aerospace Computational Modeling Laboratory
407-803, 501 Jinju-daero, Jinju, Gyeongnam 52828, Republic of Korea

[c]Korea Aerospace Industries, Ltd, 78, Gongdanro 1-ro, Sanam-myeon, Sacheon, Gyeongsangnam-do, Republic of Korea

[+]These authors contributed equally to this study.
*Co-corresponding authors: Hakjin Lee, Rho Shin Myong, and Youngwoo Nam
E-mail: hlee@gnu.ac.kr, myong@gnu.ac.kr and ywnam@gnu.ac.kr

Abstract

We propose a wing-shaped composite structure that uses an electroless nickel-plated carbon fabric as an electro-thermal heating element, thus improving the electrical and thermal properties. The results showed that the electro-thermal conversion efficiency increased from 0.064 to 0.054 W/°C with increasing plating thickness and weight percentage of the nickel particles deposited. The experiments demonstrated that the surface temperature of the wing-shaped composite could be heated up to 87.9 °C within 1000 s at an applied power density of 2.11 kW/m^2. The measurement results agreed well with those of the coupled electro-thermal simulations of heating elements related to a resistance heating phenomenon via an electro-thermal conversion, and it validated the heating performance. In addition, the nickel-plated carbon fabric as a heating element for the leading edge of the wing-shaped model was examined using a multiphysics de-icing simulation under actual icing conditions from a practical perspective. Most of the icing was removed by applying a power density of 2.7 kW/m^2 for 600 s to the wing-shaped composite structure. An interlaminar shear strength (ILSS) test was performed to verify the mechanical performance in terms of structural integrity. This practical approach could efficiently offer a desirable solution for the multifunctional de-icing composite field.

Keywords: Multifunctional de-icing composite, Nickel-plated carbon fabric, Multiphysics de-icing simulation, Electro-thermal properties, Mechanical properties.

1. Introduction

Ice accretion and formation on the surface of an aircraft poses a significant safety risk during aircraft operation [1, 2]. Ice accretion on major components, such as the wings and propeller of an aircraft or the rotor blades of a helicopter, can cause an increase in drag, a decrease in lift, a change in moment characteristics, etc., which significantly affect the performance of these components [3–5]. Therefore, there is ongoing research on electro-thermal anti-icing/de-icing methods that have high thermal efficiencies and low power requirements and also provide structural stability to effectively prevent or remove icing on the surfaces of the major components of an aircraft [6–9]. Numerous studies have predicted ice formation on the surface of an aircraft [10–13] and measured the heating performance [14–19]. These studies have analyzed the icing phenomenon on surfaces and complex heat transfer phenomena, such as heat exchange, when air or supercooled droplets collide with a surface. Currently, several studies have mainly focused on electro-thermal heating elements that utilize multifunctional composite materials [20–23]. Table 1 lists the performances of the electro-thermal heating elements reported in literature. Carbon fabrics have been actively investigated as potential multifunctional composite materials owing to their high specific strength, specific stiffness, thermal efficiency, and heating performance compared to metals [24–26]. However, carbon fabrics have high electrical resistances and low electrical conductivities owing to their turbostratic graphite structure, which limits their use as heating elements [27]. Recent studies have shown that the electro-thermal properties induced by conductive particles can improve the heating performance of carbon, e.g., in heating films that use carbon nanotubes [28–30] or graphene dispersions [31–33], heating elements that use discontinuous carbon fabrics [34], and the improvement of the electrical and thermal conductivities of carbon fabrics through metal plating [35–37]. However, the existing methods for improving the electro-thermal properties of carbon have limitations in that they produce nonuniform electro-thermal characteristics and their manufacturing process is complicated. To overcome these limitations, many studies have investigated the process of electroless metal plating [38, 39] to achieve favorable electro-thermal properties. This process does not use electricity, and it plates metal ions on the surface of a fiber via oxidation and reduction in an aqueous solution. Certain electrical and thermal properties can be obtained by uniformly coating a fiber surface with metals such as nickel, copper, or silver [40–42]. In particular, nickel provides the advantages of excellent corrosion and abrasion resistance due to the formation of a passive film [43]. In addition, its high conductivity can improve the electrical properties and heating performances of carbon fabrics through electroless plating [44]. In this study, we proposed a wing-shaped composite structure that employed an electroless nickel-plated carbon fabric, achieving high-efficiency electro-thermal heating elements with enhanced electrical and thermal properties; the proposed structure concept is shown in Fig. 1. In addition, multiphysics de-icing simulations were investigated to obtain a better understanding of the de-icing performance in actual atmospheric icing conditions. Furthermore, we conducted an interlaminar shear strength (ILSS) test to evaluate the mechanical performance related to the interfacial adhesion properties between the nickel-plated fabric and polymer matrix, which indicated their feasibility in terms of structural integrity.

2. Materials and methods

2.1. Nickel-plated carbon fabric

A pristine carbon fabric, purchased from Minhu Composite Co. Ltd., was coated with nickel via electroless plating to enhance its electrical and thermal properties [45]. Electroless plating was performed on the mass production (width = 1.5 m, length = 100 m) from Ajin Electron Co. Ltd. Fig. 2(a) shows the electroless plating process and the scanning electron microscopy (SEM; MIRA3 LMU, TESCAN, Czechia) images of the nickel-plated carbon fabrics. A uniform nickel layer was deposited on the surface of the pristine carbon fabric. Fig. 2(b) shows the results of the energy dispersive spectroscopy (EDS; JSM-7610F, JEOL, Japan) of the nickel-plated carbon fabric of sample #3, indicating the elemental nickel composition in terms of weight percentage and atomic ratio. No nickel was detected in the pristine carbon fabric; however, the nickel content increased to 86.43 wt. % after electroless plating. Table 2 shows the composition of the pristine and nickel-plated carbon fabrics of samples #1–#3. Fig. 2(c) shows the results of the X-ray photoelectron spectroscopy (XPS; Nexsa, Thermo Fisher Scientific, USA) of the pristine and nickel-plated carbon fabrics. The nickel-plated carbon fabrics (samples #1, #2, and #3) showed a nickel peak at 856.1 eV, whereas no nickel peak was observed in the pristine carbon fabric. We used X-ray diffraction (XRD; Ultima IV, Rigaku, Japan) to perform a phase analysis on the nickel-plated carbon fabrics, and the results are shown in Fig. 2(d). We did not observe any nickel peaks in the pristine carbon fabric. However, nickel peaks were observed in the nickel-plated carbon fabrics at 2θ = 43.5°, 50.6°, and 74.3°. Table 3 shows the electrical and thermal properties of the nickel-plated carbon fabrics for different thickness of the plated nickel. The electrical and thermal properties were measured using the four-point probe method (FPP; MST 5500B, MSTECH, Republic of Korea) and laser flash analysis (LFA; LFA 467 HyperFlash, NETZSCH, Germany), respectively. These properties were predominantly determined by the thickness and composition of nickel, which were controlled by the speed of the roller in the plating bath and the plating time [46]. The thickness of the plated-nickel was measured via X-ray fluorescence (XRF; XRF-2000R, Micro Pioneer, Republic of Korea). From these results, it was evident that the electrical and thermal properties were enhanced with increasing the nickel plating thickness. The electrical and thermal conductivities of the pristine carbon fabric were 5.506×10^3 S/m and 0.623 W/m·K, respectively, and those of sample #3, having the highest nickel plating thickness, were 19.16×10^3 S/m and 0.833 W/m·K, respectively.

2.2. Heating mechanism

We used nickel-plated carbon fabrics with low resistances and high electro-thermal conductivities as heating elements to achieve a high heating capacity. The heating mechanism was based on resistance heating via electro-thermal conversion. When an electric current passes through a conductive solid or liquid, electrons move and collide with nuclei. At this point, heat is generated by the conversion of kinetic energy into thermal energy. Electro-thermal heating is advantageous because the amount of heat generated can be controlled by adjusting the applied voltage and current, and heat is generated regardless of the external conditions. The amount of heat generated by electro-thermal heating is expressed using Joule's law [47]

$$V = IR, \tag{1}$$

$$H = I^2 Rt. \tag{2}$$

In the above equations, V represents the applied voltage (V), I represents the applied current (A), R represents the resistance (Ω), H represents the amount of heat (W), and t represents time (s).

2.3. Numerical methods

The heating performances of the nickel-plated carbon fabrics and wing-shaped composite structure were verified by performing computational analysis using Abaqus/CAE 6.14-2 (Dassault Systèmes SE, France). We used a coupled electro-thermal analysis that simultaneously considered the thermal and electrical behaviors of the heating elements [20, 48, 49]. Introducing Ohm's law, the governing conservation of electric charge equation is given in Eq. (3), where φ is the potential, $\boldsymbol{\sigma}^{\mathbf{E}}$ is the electrical conductivity, r_c is the internal volumetric current source per unit volume, and J is the current density entering the control volume across S.

$$\int_V \frac{\partial \delta\varphi}{\partial \mathbf{x}} \cdot \boldsymbol{\sigma}^{\mathbf{E}} \cdot \frac{\partial \varphi}{\partial \mathbf{x}} dV = \int_S \delta\varphi \, J \, dS + \int_V \delta\varphi \, r_c \, dV \tag{3}$$

The thermal energy conservation equation for heat flow is given by Eq. (4), where ρ is density of the material, $\dot{U}$ is the internal energy, $\mathbf{k}$ is the thermal conductivity matrix, q is the heat flux per unit area of the body, and r is the heat generated within the body [50].

$$\int_V \rho \dot{U} \delta\theta dV + \int_V \frac{\partial \delta\theta}{\partial \mathbf{x}} \cdot \mathbf{k} \cdot \frac{\partial \theta}{\partial \mathbf{x}} dV = \int_V \delta\theta \, r \, dV + \int_S \delta\theta \, q \, dS \tag{4}$$

Actual icing conditions involve phenomena that are difficult to consider in heating tests conducted on the ground, such as the heat exchange that occurs when air or supercooled droplets collide with an aircraft. We used FENSAP-ICE for a multiphysics de-icing simulation to verify the de-icing performance of the wing-shaped composite structure under actual icing conditions. The multiphysics de-icing analysis included simulations of external air flow and droplet impingement and also an unsteady conjugate heat transfer (CHT) simulation of electro-thermal de-icing as shown in Fig. 3. For the CHT analysis, the simulations of ice accretion, heat transfer analysis between a water film and multilayer heat conduction, and ice layer re-meshing were conducted iteratively. The Reynolds-averaged Navier–Stokes equations were used to evaluate the flow field around the wing-shaped composite structure with heating elements. The Spalart–Allmaras turbulence model was employed. We used an Eulerian droplet impingement model to calculate the supercooled droplet field in the atmosphere and considered the multiphase model proposed by Bourgault *et al.* [51–53]. Air and droplets were mixed in this model. The attachment of the droplets to the surface and ice accretion could be described using a continuity equation for the film thickness and energy equation for the temperature given in Eqs. (5) and (6), respectively [54–56].

$$\rho_w \left[\frac{\partial h_f}{\partial t} + \nabla \cdot (\overline{\mathbf{U_f}} h_f) \right] = U_\infty LWC\beta - \dot{m}_{evap} - \dot{m}_{ice}, \tag{5}$$

$$\begin{aligned} \rho_w \left[\frac{\partial h_f C_w T_f}{\partial t} + \nabla \cdot (\overline{\mathbf{U_f}} h_f C_w T_f) \right] = {} & \left[C_w T_{d,\infty} + \frac{|\mathbf{U}_d|^2}{2} \right] U_\infty LWC\beta \\ & -0.5(L_{evap} + L_{subl})\,\dot{\mathrm{m}}_{evap} + (L_{fusion} - C_{ice} T_f)\,\dot{\mathrm{m}}_{ice} \\ & +\sigma\varepsilon(T^4_\infty - T_f{}^4) + C_h(T_f - T_{ice.rec}) + \mathrm{Q}_{de-icing}\,. \end{aligned} \tag{6}$$

Here, ρ_w is the water density, and C_w and C_{ice} are the specific heats at constant pressure for water and ice, respectively. $\overline{\mathbf{U_f}}$ and h_f are the velocity and thickness of the water film, respectively. T_f is the equilibrium temperature, $\mathbf{U_d}$ is the velocity of droplet, σ is the solid emissivity, ε is the Boltzmann constant, L_{evap}, L_{subl}, and L_{fusion} are the latent heats of evaporation, sublimation, and fusion, respectively, β is the rate of collection efficiency, $\dot{m}_{evap}$ and $\dot{m}_{ice}$ are the mass fluxes during evaporation and icing, respectively, C_h is the convective heat transfer coefficient, T_∞ and $T_{d,\infty}$ are the liquid water contents (LWC), and U_∞ represents the user-defined phase and droplet variables. The first term on the right side of Eq. (6) denotes the heat transfer that occurred when supercooled droplets collided with a surface, the second term denotes the heat transfer that occurred when droplets evaporated, the third term denotes the heat transfer due to ice accretion, and the remaining terms denote radiation and convection heat transfer [57, 58].

3. Electro-thermal heating performance

3.1. Measurement of the electro-thermal heating performance

The heating performance related to the temperature distribution on the surface on the 40 × 40 mm^2 nickel-plated carbon fabrics as heating elements, with copper foil attached as electrodes to both ends of the fabrics using a highly conductive silver paste (ELCOAT A-200; CANS, Republic of Korea), was measured using an infrared camera (IR camera; FLIR E53, Teledyne FLIR LLC, USA), as shown in Fig. 4(a) [59–61]. Fig. 4(b) shows the thermal images captured on the surface of the pristine carbon fabric and samples #1, #2, and #3 as heating elements by applying a constant voltage of 1.5 V for 5 min. The maximum temperatures of the surface of the pristine carbon fabric and samples #1, #2, and #3 were 103.6 ℃, 114.7 ℃, 138.6 ℃, and 148.2 ℃, respectively, as shown in Fig. 4(c). From the measurements, it was found that the nickel-plated carbon fabric functioned well as sample #3 especially was heated up to 100 ℃ at a heating rate of 8.25 ℃ /sec. The equilibrium temperature in accordance with the thermal dissipation process as heat loss resulting from the surrounding conditions may be determined by Joule's law [47]. In particular, the surface temperature of sample #3 was 43.1% higher than that of the pristine carbon fabric. It appears to be evident that the amount of applied current increased due to the enhanced electrical conductivity, which corresponded to the amount of plating thickness and weight percentage of the nickel particles. The electro-thermal conversion efficiency was measured to provide a more comprehensive understanding of the nickel-plated carbon fabric used in this study. It was obtained using the following equation, and the values are shown in Table 4 [62, 63].

$$h_{r+c} = \frac{I_c V_0}{T_m - T_0} \tag{7}$$

Here, h_{r+c} is the electro-thermal conversion efficiency, a smaller value of which denotes a better conversion efficiency. I_c is the steady state current, V_0 is the applied voltage, and T_0 and T_m are the initial and maximum surface temperatures, respectively. Sample #3 with a maximum temperature of 148.2 °C exhibited the highest electro-thermal conversion efficiency of 0.054 W/°C. Thus, sample #3 was selected to demonstrate the wing-shaped composite structure in this study.

3.2. Coupled electro-thermal analysis of the heating element

A coupled electro-thermal analysis was conducted to verify the high heating capacity of the electro-thermal heating element proposed in this study. The measured values of the steady-state current, applied voltage, and initial surface temperature, as listed in Table 4, were used for the simulation, and the computational grid consisted of 400 cells of 2 × 2 mm^2 each. A voltage of 1.5 V and the current measured during the heating test were applied to the heating element as simulation conditions. In addition, room temperature was considered as the surface film condition with the sink and initial surface temperatures of 28 °C. We compared the surface temperature obtained from the heating test and coupled electro-thermal simulation for 300 s. Fig. 5(a) shows the variation in the surface temperature with respect to time. Fig. 5(b) presents the simulation and test results for sample #3 for the steady state temperature distribution along the transverse direction. The overall distribution of the surface and maximum temperatures agreed well with the measurements, although the magnitudes of the top and bottom regions were slightly overestimated. The simulation results showed that the surface temperature at the outermost point was 143.4 °C, the maximum surface temperature at the center was 148.4 °C, and the overall surface temperature was 147–148 °C. The measurements showed that the surface temperature at the outermost point was 120 °C and the maximum surface temperature at the center was 148.2 °C. The temperature at a transverse position of 12–30 mm was 144–146 °C and that at transverse positions of 0–12 mm and 30–40 mm was 120–138 °C. Thus, the surface temperature decreased as the distance from the center of the specimen increased. The difference between the surface temperatures at the center and outermost points was approximately 29 °C. This difference was due to heat loss caused by the contact between the fabric structure and air [64–66].

4. Leading edge of the wing-shaped composite

4.1. Fabrication and measurement

As mentioned in Section 2.1, a nickel-plated carbon fabric prepared using electroless nickel plating was presented to obtain improved electrical and thermal properties, providing the heating elements with high electro-thermal conversion efficiencies. The stacking sequence of the proposed wing-shaped composite used in this study is shown in Fig. 6(a). The proposed structure with heating elements was designed by controlling the stacking sequence profiles. One layer of the nickel-plated carbon fabric (t = 0.15 mm) as a heating element was embedded between the two plies (t = 0.3 mm) of glass/epoxy to satisfy the level of electrical insulation with adhesion resistance. The carbon/epoxy layers in accordance with thickness thermal transfer as load-bearing capacity was layered on both sides of the heating element with two plies (t = 0.3 mm) and six plies (t = 1.65 mm), respectively, considering their effective thermal transfer in the perpendicular direction. The six plies (t = 0.9 mm) of glass/epoxy with respect to the heat sink of the top and bottom layers were layered to provide a precise protection against ignition while maintaining uniform heat. Fig. 6(b) summarizes the fabrication process flow of the leading edge of the wing-shaped composite with the nickel-plated carbon fabrics developed in this study as the electro-thermal heating elements. After completing the lay-up for the wing-shaped model, the layered sample was vacuum-bagged and cured in an autoclave curing cycle (120 min at 130 °C under a pressure of 7 atm). The total thickness of the fabricated wing-shaped composite structure was 4.75 mm. The heating behavior with regards to five heating elements inserted at different positions on the wing-shaped composite was characterized using a test setup as shown in Fig. 7. The wing-shaped composite was connected to a DC electrical power supply (DC power supply; TS3030A, TOYOTECH, Republic of Korea), and the temperature distribution related to the quantitative assessment of the image on the surface of the wing-shaped composite was monitored using an infrared camera. Five heating elements were positioned as shown in Fig. 8(a). Figs. 8(b–f) show the temperature profiles and infrared images of the wing-shaped composite for five heating element positions within 1000 s with a voltage of 12 V. It can be noted that the heating elements #1, #2, #3, #4, and #5 were gradually heated up to 87.3 °C, 86.6 °C, 87.9 °C, 88.1 °C, and 86.9 °C, respectively, under a power voltage of approximately 2.06–2.14 kW/m^2, demonstrating a good and uniform electro-thermal performance. The five heating element positions with respect to current, power density, and maximum temperature are presented in Table 5. Based on these experimental results, it was verified that the nickel-plated carbon fabric with a high electro-thermal conversion efficiency functioned well as the heating element without the use of nanocarbon fillers [67, 68], nanoparticles [69, 70], or hybrid fillers consisting of graphite, expanded graphite, and Cu [71] to achieve favorable electro-thermal properties. Many studies had focused on the effect on the electro-thermal properties with respect to highly conductive materials. However, these approaches faced certain limitations in terms of practical application, namely composite material with dispersed nanoparticles could lead to inhomogeneous mechanical and electrical properties owing to the high viscosity of the polymer matrix and the fabrication processes were also complicated. Hence, the present study attempts to overcome these limitations by demonstrating that the nickel-plated carbon fabric has high electro-thermal conversion efficiency and heating performance and can be used in the wing-shaped composite without the use of nanoparticles, indicating its feasibility and applicability from a practical perspective.

4.2. Mechanical performance

To examine the interlaminar shear behavior of the nickel-plated carbon fabric layer on the composite, the pristine and nickel-plated carbon/epoxy composites (sample #3) were analyzed according to ASTM D-2344 standards, as shown in Fig. 9(a). All interlaminar shear test specimens were prepared with the same stacking sequence and configuration as discussed in Section 4.1, including a glass fabric as an electrical insulating layer. The ILSS was obtained using the following equation.

$$P^{sbs} = 0.75 \times \frac{P_m}{b \times h} \tag{8}$$

Here, P^{sbs} is the ILSS (MPa), P_m is the maximum load (N), and b and h are the width (mm) and thickness (mm) of the specimen, respectively. The length, average width, and thickness of the fabricated test specimens were 18 mm, 6 mm, and 3 mm, respectively. The test results for the pristine and nickel-plated carbon/epoxy composites showed that the ILSSs were 28.7 MPa and 28.4 MPa, respectively, as shown in Fig. 9(b). Furthermore, a typical failure mode was acceptable for all the samples with respect to the test standard not only corresponding to the similar strength affected by interfacial adhesion properties between the nickel particles deposited on the carbon fabric and matrix but also offered structural integrity approaches in terms of their durability and feasibility.

4.3. Coupled electro-thermal simulation results

A coupled electro-thermal analysis of the wing-shaped composite structure was conducted, and the simulation results were compared with those of the heating test to verify the heating performance of the structure. Heating element #3 of the wing-shaped composite structure was considered and 12 V were applied for 1000 s to obtain a steady state temperature distribution on the heating element surface. The computational grid consisted of 280,765 cells of 3 × 3 mm^2 each. A voltage of 12 V and a current of 7.4 A were applied to heating element #3 as the simulation conditions. For the finite element method (FEM) simulation, the surface contact conditions were imposed on each layer of the wing-shaped composite to consider heat transfer between the overlapping layers. In addition, the surface film conditions with a sink temperature of 15 ℃ were applied to the outermost surfaces to consider the heat transfer between the ambient air and the heating element. The temperature distribution on the surface of the wing-shaped composite structure is presented in Fig. 10(a), and the predicted result of the temperature distribution was in good agreement with the measured data as shown in Fig. 8(d). Fig. 10(b) shows a detailed comparison between the surface temperatures obtained from the FEM simulation and heating test results. It can be observed that the simulation results of the temperature variation along the transverse direction agreed well with the measurements. The maximum temperature was observed at a transverse position of 150 mm corresponding to the center of heating element #3 of the wing-shaped composite. The predicted and measured maximum temperatures were 88.4 ℃ and 87.9 ℃, respectively. The discrepancy between the maximum temperatures obtained during the FEM simulation and heating test was only 0.5 ℃. Results showed that the wing-shaped composite with the nickel-plated carbon fabric proposed in this study was capable of applying an electro-thermal heating element for applications in de-icing systems.

4.4.Multiphysics de-icing simulation results

Analysis of ice accretion on the wing-shaped composite with a nickel-plated carbon fabric were conducted under an actual icing environment using Ansys FENSAP-ICE 2019 R1 (Ansys Inc., USA) to predict the shape of the ice. Fig. 11 shows the computational domain and boundary conditions for ice accretion and multiphysics de-icing simulations. To model the heating elements placed on the leading edge of wing-shaped composite, both the external wall, exposed to the external flow, and solid wall were considered. The computational grid consisted of 158,006 and 75,624 cells for the external and solid walls, respectively. The pressure far-field boundary condition was applied to the boundaries of the external flow field, and the solid wall boundary condition was imposed on the surfaces of external and solid walls. The simulation conditions for the ice accretion analysis were determined from Appendix C in the Federal Aviation Regulation Part 25 of the Federal Aviation Administration [72]. Two cases were selected among the various flow conditions for ice accretion: Case 1 was the condition that generated the largest amount of ice, and Case 2 was the condition wherein ice accretion had the most influence on the variation in the lift and drag coefficients [73–75]. The details of the flow conditions for the icing simulation are listed in Table 6. Fig. 12 shows the collection efficiencies for Cases 1 and 2. After droplet impingement on the wing, collection efficiency was symmetrically distributed in Case 1, whereas it was distributed more widely on the lower surface of the leading edge in Case 2 owing to an angle of attack of 4°. When exposed to icing conditions for 600 s without activating the de-icing system, ice accretion occurred as shown in Fig. 13. Icing accrued symmetrically in Case 1, whereas it accrued in a horn-ice shape that spread widely on the lower surface of the leading edge in Case 2 owing to the angle of attack of 4°. We also performed a multiphysics de-icing simulation at a constant power density for the heating element (2.7 kW/m^2) during exposure to atmospheric icing conditions for 600 s. The surface temperature of the leading edge increased to 8 ℃ and 10 ℃ in Cases 1 and 2, respectively. Although there existed a difference of 10 ℃ between the atmospheric temperatures in Cases 1 (-16 ℃) and Cases 2 (-6 ℃), only a 2 ℃ difference existed between the increase in the surface temperature caused by the heating element in both cases. This is because aerodynamic heating and droplet impingement position varies depending on the angle of attack [14, 76]. In Case 1, the angle of attack was 0° and the thermal energy was primarily generated by impingement between the air and droplets on the leading edge. In contrast, the angle of attack was 4° in Case 2 and the thermal energy was primarily generated by impingement between the air and droplets on the lower surface of the leading edge. Ice accretions on the surface of the wing with and without the de-icing system proposed in this study are compared in Figs. 14(a) and 14(b). Notably, the de-icing system successfully removed most of the icing, although ice accretion associated with liquid runback along the lower surface was observed. Runback ice was generated behind heating element #3, where the surface temperature was below 0 °C. Runback ice can be removed entirely by relocating or increasing the number of heating elements in the wing-shaped composite structure or by optimizing the heating sequence.

5. Conclusions

In this paper, the leading edge of a wing-shaped multifunctional composite structure with a nickel-plated carbon fabric as a heating element, providing excellent electrical and thermal properties, was presented to achieve high electro-thermal conversion efficiency and heating performance. The heating element level test related to the heating performance increased as the plating thickness and weight percentage of the nickel particles deposited was increased, generating a value 43.1% higher than that of the pristine carbon fabric. The results obtained from the electro-thermal heating test of the wing-shaped composite with heating elements were in good qualitative agreement with the corresponding simulation results, demonstrating a surface temperature of 87.9 °C with a power density of 2.11 kW/m^2. To simulate the flight conditions in an actual atmospheric icing environment, we performed a multiphysics de-icing simulation under the conditions wherein a large amount of icing was generated, which strongly influenced the variation in the lift and drag performances. We examined the ice accretion shapes on the leading edge. Most of the icing was removed at a relatively low power density of 2.7 kW/m^2. The ILSS results of the nickel-plated carbon/epoxy composite were comparable with those of a pristine carbon/epoxy composite. From these results, it can be concluded that both the insulating layer and heating element did not significantly affect the interfacial adhesion properties. This suggests that the composite structure with a nickel-plated carbon fabric as the heating element can efficiently provide a practical approach that can be used in applications such as wind blades, the rotor blades of rotorcrafts, and air intakes as well as aircraft wing composites.

Acknowledgments

This work was supported by the National Research Foundation of Korea (NRF) grant funded by the Ministry of Science and ICT (NRF-2017R1A5A1015311). This work was supported by the development of the IPS functional composite structure of Korea Aerospace Industries, LTD. (CT20050855RND2020)

References

[1] Landsberg B. Safety advisor: aircraft icing. AOPA Air Safety Foundation, 2008.

[2] Jin W. Numerical Investigation of Icing Effects on Dynamic Inlet Distortion. Int J Aeronaut Sp Sci 2018;19:354–62. https://doi.org/10.1007/s42405-018-0044-0.

[3] Ahn GB, Jung KY, Myong RS, Shin HB, Habashi WG. Numerical and experimental investigation of ice accretion on rotorcraft engine air intake. J Aircr 2015;52:903–9. https://doi.org/10.2514/1.c032839.

[4] Thomas SK, Cassoni RP, MacArthur CD. Aircraft anti-icing and de-icing techniques and modeling. J Aircr 1996;33:841–54. https://doi.org/10.2514/3.47027.

[5] Lynch FT, Khodadoust A. Effects of ice accretions on aircraft aerodynamics. Prog Aerosp Sci 2001;37:669–767. https://doi.org/10.1016/s0376-0421(01)00018-5.

[6] Kind RJ, Potapczuk MG, Feo A, Golia C, Shah AD. Experimental and computational simulation of in-flight icing phenomena. Prog Aerosp Sci 1998;34:257–345. https://doi.org/10.1016/s0376-0421(98)80001-8.

[7] Ding L, Chang S. Evaluation of inflight deicing performance for designed electrothermal systems with experimental verification. J Aircr 2020;57:156–66. https://doi.org/10.2514/1.c035524.

[8] Mu Z, Lin G, Shen X., Bu X, Zhou Y. Numerical simulation of unsteady conjugate heat transfer of electrothermal deicing process. Int J Aerosp Eng 2018;2018:1–16.

https://doi.org/10.1155/2018/5362541.

[9] Shinkafi A, Lawson C. Enhanced Method of Conceptual Sizing of Aircraft Electro-Thermal De-icing System. Int J Aerosp Mech Eng 2014;8:1065–72. https://doi.org/10.5281/zenodo.2661308.

[10] Cao Y, Ma C, Zhang Q, Sheridan J. Numerical simulation of ice accretions on an aircraft wing. Aerosp Sci Technol 2012;23:296–304. https://doi.org/10.1016/j.ast.2011.08.004.

[11] Myers TG. Extension to the Messinger model for aircraft icing. AIAA J 2001;39:211–8. https://doi.org/10.2514/3.14720.

[12] Raj LP, Lee JW, Myong RS. Ice accretion and aerodynamic effects on a multi-element airfoil under SLD icing conditions. Aerosp Sci Technol 2019;85:320–33. https://doi.org/10.1016/j.ast.2018.12.017.

[13] Ghenai C, Lin CX. Verification and validation of NASA LEWICE 2.2 icing software code. J Aircr 2006;43:1253–8. https://doi.org/10.2514/1.18977.

[14] Pourbagian M, Habashi WG. Aero-thermal optimization of in-flight electro-thermal ice protection systems in transient de-icing mode. Int J Heat Fluid Flow 2015;54:167–82. https://doi.org/10.1016/j.ijheatfluidflow.2015.05.012.

[15] Meier O, Scholz D. A handbook method for the estimation of power requirements for electrical de-icing systems. DLRK, Hamburg; 2010. p. 31.

[16] Yaslik AD, De Witt KJ, Keith TG, Boronow W. Three-dimensional simulation of electrothermal deicing systems. J Aircr 1992;29:1035–42. https://doi.org/10.2514/3.46281.

[17] Hedde T, Guffond D. ONERA three-dimensional icing model. AIAA J 1995;33:1038–45. https://doi.org/10.2514/3.12795.

[18] Chen L, Zhang Y, Wu Q. Heat transfer optimization and experimental validation of anti-icing component for helicopter rotor. Appl Therm Eng 2017;127:662–70. https://doi.org/10.1016/j.applthermaleng.2017.07.169.

[19] Battisti L, Fedrizzi R. 2D numerical simulation of a wind turbine de-icing system, using cycled heating. Wind Eng 2007;31:33–42. https://doi.org/10.1260/030952407780811375.

[20] Zhang Z, Chen B, Lu C, Wu H, Wu H, Jiang S, et al. A novel thermo-mechanical anti-icing/de-icing

system using bi-stable laminate composite structures with superhydrophobic surface. Compos Struct 2017;180:933–43. https://doi.org/10.1016/j.compstruct.2017.08.068.

[21] Chu H, Zhang Z, Liu Y, Leng J. Self-heating fiber reinforced polymer composite using meso/macropore carbon nanotube paper and its application in deicing. Carbon 2014;66:154–63. https://doi.org/10.1016/j.carbon.2013.08.053.

[22] Luo J, Lu H, Zhang Q, Yao Y, Chen M, Li Q. Flexible carbon nanotube/polyurethane electrothermal film. Carbon 2016;110:343–349. https://doi.org/10.1016/j.carbon.2016.09.016.

[23] Liu P, Liu L, Jiang K, Fan S. Carbon-nanotube-film microheater on a polyethylene terephthalate substrate and its application in thermochromic displays. Small 2011;7:732–6. https://doi.org/10.1002/smll.201001662.

[24] Falzon BG, Robinson P, Frenz S, Gilbert B. Development and evaluation of a novel integrated anti-icing/de-icing technology for carbon fibre composite aerostructures using an electro-conductive textile. Compos Part A Appl Sci Manuf 2015;68:323–35. https://doi.org/10.1016/j.compositesa.2014.10.023.

[25] Yao X, Hawkins SC, Falzon BG. An advanced anti-icing/de-icing system utilizing highly aligned carbon nanotube webs. Carbon 2018;136:130–8. https://doi.org/10.1016/j.carbon.2018.04.039.

[26] Zheng X, Kim SM, Park CW. Enhancement of thermal conductivity of carbon fiber-reinforced polymer composite with copper and boron nitride particles. Compos Part A Appl Sci Manuf 2019;121:449–56. https://doi.org/10.1016/j.compositesa.2019.03.030.

[27] Das TK, Ghosh P, Das NC. Preparation, development, outcomes, and application versatility of carbon fiber-based polymer composites: a review. Adv Compos Hybrid Mater 2019;2:214–33. https://doi.org/10.1007/s42114-018-0072-z.

[28] Yao X, Falzon BG, Hawkins SC, Tsantzalis S. Aligned carbon nanotube webs embedded in a composite laminate: A route towards a highly tunable electro-thermal system. Carbon 2018;129:486–94. https://doi.org/10.1016/j.carbon.2017.12.045.

[29] Yoon Y-H, Song J-W, Kim D, Kim J, Park J-K, Oh S-K, et al. Transparent film heater using single-walled carbon nanotubes. Adv Mater 2007;19:4284–7.

https://doi.org/10.1002/adma.200701173.

[30] Kim DJ, Lee H-C, Woo JY, Han C-S. Thermal behavior of transparent film heaters made of single-walled carbon nanotubes. J Phys Chem C 2010;114:5817–21. https://doi.org/10.1021/jp910799a.

[31] Tian M, Hao Y, Qu L, Zhu S, Zhang X, Chen S. Enhanced electrothermal efficiency of flexible graphene fabric Joule heaters with the aid of graphene oxide. Mater Lett 2019;234:101–4. https://doi.org/10.1016/j.matlet.2018.09.078.

[32] Sui D, Huang Y, Huang L, Liang J, Ma Y, Chen Y. Flexible and transparent electrothermal film heaters based on graphene materials. Small 2011;7:3186–92. https://doi.org/10.1002/smll.201101305.

[33] Vertuccio L, De Santis F, Pantani R, Lafdi K, Guadagno L. Effective de-icing skin using graphene-based flexible heater. Compos B Eng 2019;162:600–10. https://doi.org/10.1016/j.compositesb.2019.01.045.

[34] Kim MS, Sung DH, Kong KG, Kim NR, Kim B-J, Park HW, et al. Characterization of resistive heating and thermoelectric behavior of discontinuous carbon fiber-epoxy composites. Compos B Eng 2016;90:37–44. https://doi.org/10.1016/j.compositesb.2015.11.037.

[35] Darvishzadeh A, Nasouri K. Manufacturing, modeling, and optimization of nickel-coated carbon fabric for highly efficient EMI shielding. Surf Coat Technol 2021;409:126957. https://doi.org/10.1016/j.surfcoat.2021.126957.

[36] Kim B-J, Choi W-K, Um M-K, Park S-J. Effects of nickel coating thickness on electric properties of nickel/carbon hybrid fibers. Surf Coat Technol 2011;205:3416–21. https://doi.org/10.1016/j.surfcoat.2010.12.007.

[37] Cao Y, Farha FI, Ge D, Liu X, Liu W, Li G, et al. Highly effective E-heating performance of nickel coated carbon fiber and its composites for de-icing application. Compos Struct 2019;229:111397. https://doi.org/10.1016/j.compstruct.2019.111397.

[38] Jang J, Ryu SK. Physical property and electrical conductivity of electroless Ag-plated carbon fiber-reinforced paper. J Mater Process Technol 2006;180:66–73.

https://doi.org/10.1016/j.jmatprotec.2006.05.003.

[39] Tzeng S-S, Chang F-Y. Electrical resistivity of electroless nickel coated carbon fibers. Thin Solid Films 2001;388:143–9. https://doi.org/10.1016/s0040-6090(01)00809-4.

[40] Yim Y-J, Rhee KY, Park S-J. Influence of electroless nickel-plating on fracture toughness of pitch-based carbon fibre reinforced composites. Compos B Eng 2015;76:286–91. https://doi.org/10.1016/j.compositesb.2015.01.052.

[41] Xu C, Liu G, Chen H, Zhou R, Liu Y. Fabrication of conductive copper-coated glass fibers through electroless plating process. J Mater Sci: Mater Electron 2014;25:2611–7. https://doi.org/10.1007/s10854-014-1919-x.

[42] Yu D, Mu S, Liu L, Wang W. Preparation of electroless silver plating on aramid fiber with good conductivity and adhesion strength. Colloid Surf A: Physicochem Eng Asp 2015;483:53–9. https://doi.org/10.1016/j.colsurfa.2015.07.021.

[43] Laszczyńska A, Tylus W, Winiarski J, Szczygieł I. Evolution of corrosion resistance and passive film properties of Ni-Mo alloy coatings during exposure to 0.5 M NaCl solution. Surf Coat Technol 2017;317:26–37. https://doi.org/10.1016/j.surfcoat.2017.03.043.

[44] Choi B-K, Choi W-K, Rhee KY, Park S-J, Seo M-K. Influence of heat treatment temperature on structure and exothermic properties of electroless Ni P plating carbon fiber heating elements. Compos B Eng 2019;167:676–82. https://doi.org/10.1016/j.compositesb.2019.03.057.

[45] Nam Y-W, Choi J-H, Lee W-J, Kim C-G. Fabrication of a thin and lightweight microwave absorber containing Ni-coated glass fibers by electroless plating. Compos Sci Technol 2017;145:165–172. https://doi.org/10.1016/j.compscitech.2017.04.009.

[46] Choi W-H, Choe H-S, Nam Y-W. Multifunctional microwave heating and absorbing honeycomb core using nickel-coated glass fabric. Compos Part A: Appl Sci Manuf 2020;138:106070. https://doi.org/10.1016/j.compositesa.2020.106070.

[47] Wang FX, Liang WY, Wang ZQ, Yang B, He L, Zhang K. Preparation and property investigation of multi-walled carbon nanotube (MWCNT)/epoxy composite films as high-performance electric heating (resistive heating) element. Express Polym Lett 2018;12:285–95.

https://doi.org/10.3144/expresspolymlett.2018.26.

[48] Koutsawa Y, Biscani F, Belouettar S, Nasser H, Carrera E. Multi-coating inhomogeneities approach for the effective thermo-electro-elastic properties of piezoelectric composite materials. Compos Struct 2010;92:964–72. https://doi.org/10.1016/j.compstruct.2009.09.041.

[49] Wang X, Casolco SR, Xu G, Garay JE. Finite element modeling of electric current-activated sintering: The effect of coupled electrical potential, temperature and stress. Acta Mater 2007;55:3611–22. https://doi.org/10.1016/j.actamat.2007.02.022.

[50] Kang YS, Park SW, Roh JS, Myong RS. Computational investigation of effects of expanded metal foils on the lightning protection performance of a composite rotor blade. Int J Aeronaut Sp Sci 2021;22:203–21. https://doi.org/10.1007/s42405-020-00288-1.

[51] Bourgault Y, Boutanios Z, Habashi WG. Three-dimensional Eulerian approach to droplet impingement simulation using FENSAP-ICE, part 1: model, algorithm, and validation. J Aircr 2000;37:95–103. https://doi.org/10.2514/2.2566.

[52] Beaugendre H, Morency F, Habashi WG. FENSAP-ICE's three-dimensional in-flight ice accretion module: ICE3D. J Aircr 2003;40:239–47. https://doi.org/10.2514/2.3113.

[53] Bourgault Y, Habashi WG, Dompierre J, Baruzzi, GS. A finite element method study of Eulerian droplets impingement models. Int J Numer Methods Fluids 1999;29:429–49. https://doi.org/10.1002/(sici)1097-0363(19990228)29:4<429::aid-fld795>3.0.co;2-f.

[54] Reid T, Baruzzi GS, Habashi WG. FENSAP-ICE: unsteady conjugate heat transfer simulation of electrothermal de-icing. J Aircr 2012;49:1101–9. https://doi.org/10.2514/1.c031607.

[55] Jung SK, Raj LP, Rahimi A, Jeong H, Myong RS. Performance evaluation of electrothermal anti-icing systems for a rotorcraft engine air intake using a meta model. Aerosp Sci Technol 2020;106:106174. https://doi.org/10.1016/j.ast.2020.106174.

[56] Bourgault Y, Beaugendre H, Habashi WG. Development of a shallow-water icing model in FENSAP-ICE. J Aircr 2000;37:640–6. https://doi.org/10.2514/2.2646.

[57] Beaugendre H, Morency F, Habashi WG. Development of a second generation in-flight icing simulation code. J Fluids Eng 2006; 128:378–87. https://doi.org/10.1115/1.2169807.

[58] Nakakita K, Nadarajah S, Habashi WG. Toward real-time aero-icing simulation of complete aircraft via FENSAP-ICE. J Aircr 2010;47:96–109. https://doi.org/10.2514/1.44077.

[59] Kong KG, Cheedarala RK, Kim MS, Roh H-D, Park Y-B, Park HW. Electrical thermal heating and piezoresistive characteristics of hybrid CuO–woven carbon fiber/vinyl ester composite laminates. Compos Part A: Appl Sci Manuf 2016;85:103–12. https://doi.org/10.1016/j.compositesa.2016.03.015.

[60] Chu K, Yun D-J, Kim DO, Park HK, Park S-H. Study of electric heating effects on carbon nanotube polymer composites. Org Electron 2014;15:2734–41. https://doi.org/10.1016/j.orgel.2014.07.043.

[61] Kandare E, Khatibi AA, Yoo SH, Wang R, Ma J, Olivier P, et al. Improving the through-thickness thermal and electrical conductivity of carbon fibre/epoxy laminates by exploiting synergy between graphene and silver nano-inclusions. Compos Part A: Appl Sci Manuf 2015;69:72–82. https://doi.org/10.1016/j.compositesa.2014.10.024.

[62] Yan J, Jeong YG. Highly elastic and transparent multiwalled carbon nanotube/ polydimethylsiloxane bilayer films as electric heating materials. Mater Des 2015;86:72–79. https://doi.org/10.1016/j.matdes.2015.07.089.

[63] Yan J, Kim BN, Jeong YG. Thermomechanical and electrical properties of PDMS/MWCNT composite films crosslinked by electron beam irradiation. J Mater Sci 2015;50:5599–608. https://doi.org/10.1007/s10853-015-9110-1.

[64] Athanasopoulos N, Sikoutris D, Panidis T, Kostopoulos V. Numerical investigation and experimental verification of the Joule heating effect of polyacrylonitrile-based carbon fiber tows under high vacuum conditions. J Compos Mater 2012;46:2153–65. https://doi.org/10.1177/0021998311430159.

[65] Athanasopoulos N, Kostopoulos V. A comprehensive study on the equivalent electrical conductivity tensor validity for thin multidirectional carbon fibre reinforced plastics. Compos B: Eng 2014;67:244–55. https://doi.org/10.1016/j.compositesb.2014.07.012.

[66] Lundström F, Frogner K, Andersson M. A method for inductive measurement of equivalent

electrical conductivity in thin non-consolidated multilayer carbon fibre fabrics. Compos B: Eng 2018;140:204–13. https://doi.org/10.1016/j.compositesb.2017.12.027.

[67] Han SJ, Chung DDL. Increasing the through-thickness thermal conductivity of carbon fiber polymer-matrix composite by curing pressure increase and filler incorporation. Compos Sci Technol 2011;71:1944–52. https://doi.org/10.1016/j.compscitech.2011.09.011.

[68] Jeong YG, An J-E. Effects of mixed carbon filler composition on electric heating behavior of thermally-cured epoxy-based composite films. Compos Part A: Appl Sci Manuf 2014;56:1–7. https://doi.org/10.1016/j.compositesa.2013.09.003.

[69] Zhang Z, Gu Y, Wang S, Li Q, Li M, Zhang Z. Enhanced dielectric and mechanical properties in chlorine-doped continuous CNT sheet reinforced sandwich polyvinylidene fluoride film. Carbon 2016;107:405–14. https://doi.org/10.1016/j.carbon.2016.05.068.

[70] Luo J, Lu H, Zhang Q, Yao Y, Chen M, Li Q. Flexible carbon nanotube/polyurethane electrothermal films. Carbon 2016;110:343–9. https://doi.org/10.1016/j.carbon.2016.09.016.

[71] Yim Y-J, Park S-J. Effect of silver-plated expanded graphite addition on thermal and electrical conductivities of epoxy composites in the presence of graphite and copper. Compos Part A: Appl Sci Manuf 2019;123:253–9. https://doi.org/10.1016/j.compositesa.2019.05.021.

[72] FAA. Part 25 - Airworthiness standards: transport category airplanes. Code of Federal Regulations, United States Federal Aviation Administration, 2019

[73] Jung SK, Shin S, Myong RS, Cho TH. An efficient CFD-based method for aircraft icing simulation using a reduced order model. J Mech Sci Technol 2011;25:703–11. https://doi.org/10.1007/s12206-011-0118-4.

[74] Fossati M, Habashi WG. Multiparameter analysis of aero-icing problems using proper orthogonal decomposition and multidimensional interpolation. AIAA J 2013;51:946–60. https://doi.org/10.2514/1.j051877.

[75] Zhan Z, Habashi WG, Fossati M. Local reduced-order modeling and iterative sampling for parametric analyses of aero-icing problems. AIAA J 2015;53:2174–85. https://doi.org/10.2514/1.j053654.

[76] Zhao Y, Chang S, Yang B, Zhang W, Leng M. Experimental study on the thermal performance of loop heat pipe for the aircraft anti-icing system. Int J Heat Mass Transf 2017;111:795–803. https://doi.org/10.1016/j.ijheatmasstransfer.2017.04.009.

Figure Captions

Figure 1 Proposed electro-thermal de-icing method for a wing-shaped composite and its practical approach in this study.

Figure 2 (a) Electroless plating process and SEM images of the nickel-plated carbon fabric; (b) EDS result of the nickel-plated carbon fabric of sample #3; (c) XPS curves; (d) XRD patterns.

Figure 3 Flowchart of the multiphysics de-icing simulation.

Figure 4 (a) Electric heating test setup; (b) images of the temperature distribution, obtained using an infrared camera, of the pristine carbon fabric and samples #1, #2, and #3; (c) temperature profiles at an applied voltage of 1.5 V.

Figure 5 Comparison between the results of the electric heating test and coupled electro-thermal simulation for the heating element: (a) temperature versus time on the heating profile for the simulation and experiment; (b) surface temperature distribution for sample #3.

Figure 6 (a) Configuration and stacking sequence of the wing-shaped composite structure used in this study; (b) fabrication process flow of the proposed wing-shaped composite.

Figure 7 Heating test setup for the leading edge of the wing-shaped composite.

Figure 8 Temperature profiles and infrared images of the wing-shaped composite: (a) heating element positions on the wing-shaped composite; (b–f) heating elements #1–#5, respectively.

Figure 9 (a) ILSS test performed using an INSTRON 5582 according to ASTM D2344 standard specifications; (b) ILSS of the pristine and nickel-plated carbon fabric/epoxy composites.

Figure 10 Coupled electro-thermal simulation results for the wing-shaped composite: (a) surface temperature contours; (b) comparison between the surface temperatures obtained from the heating test and simulation results.

Figure 11 Computational domain and boundary conditions for the multiphysics de-icing simulation.

Figure 12 Comparison between the collection efficiencies on the wing during each flight condition listed in Table 6.

Figure 13 Comparison between the shapes of the ice on the wing during each flight condition listed in Table 6.

Figure 14 Comparison between the multiphysics de-icing simulation results with and without the heating element for the flight conditions listed in Table 6: (a) Case 1; (b) Case 2.

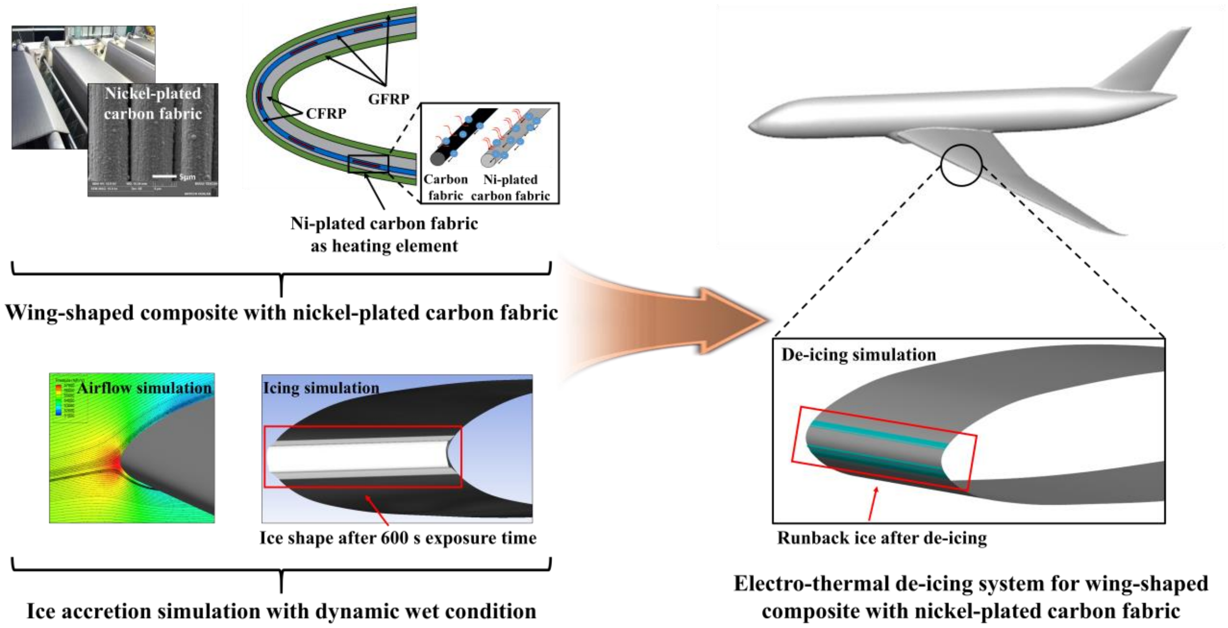
Nickel-plated carbon fabric
5μm
GFRP
CFRP
Carbon fabric
Ni-plated carbon fabric
Ni-plated carbon fabric as heating element
Wing-shaped composite with nickel-plated carbon fabric
Airflow simulation
Icing simulation
Ice shape after 600 s exposure time
Ice accretion simulation with dynamic wet condition
De-icing simulation
Runback ice after de-icing
Electro-thermal de-icing system for wing-shaped composite with nickel-plated carbon fabric

Fig. 1.

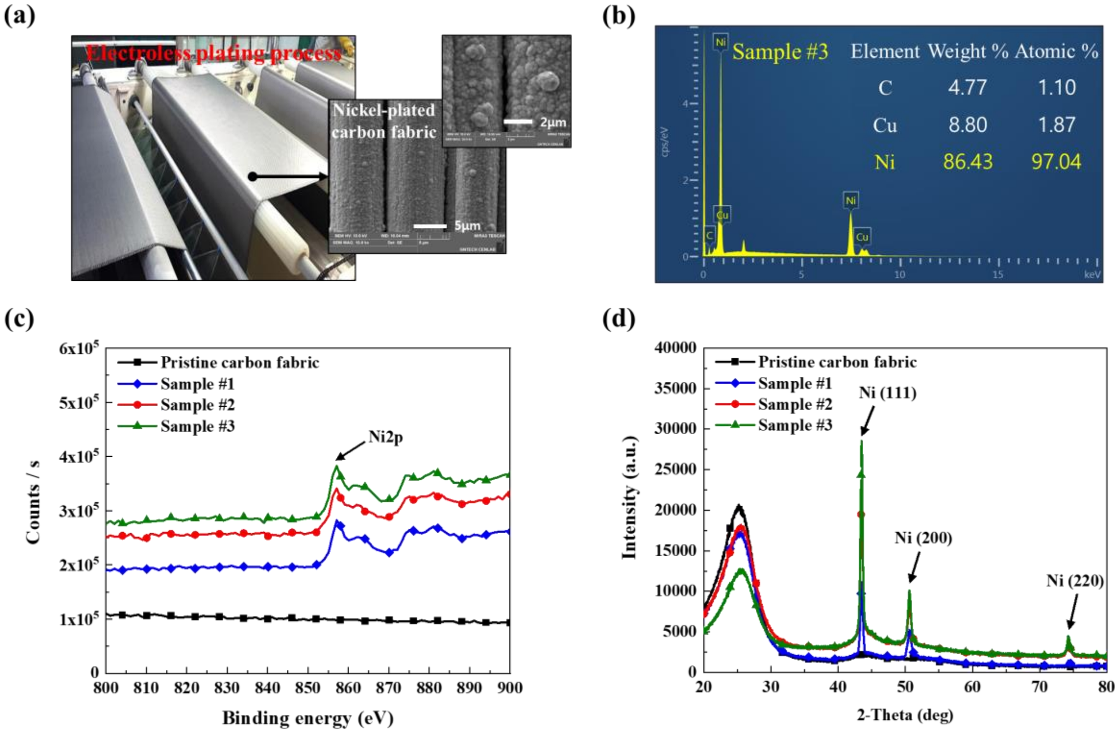

Sample #3

Element	Weight %	Atomic %
C	4.77	1.10
Cu	8.80	1.87
Ni	86.43	97.04

Fig. 2.

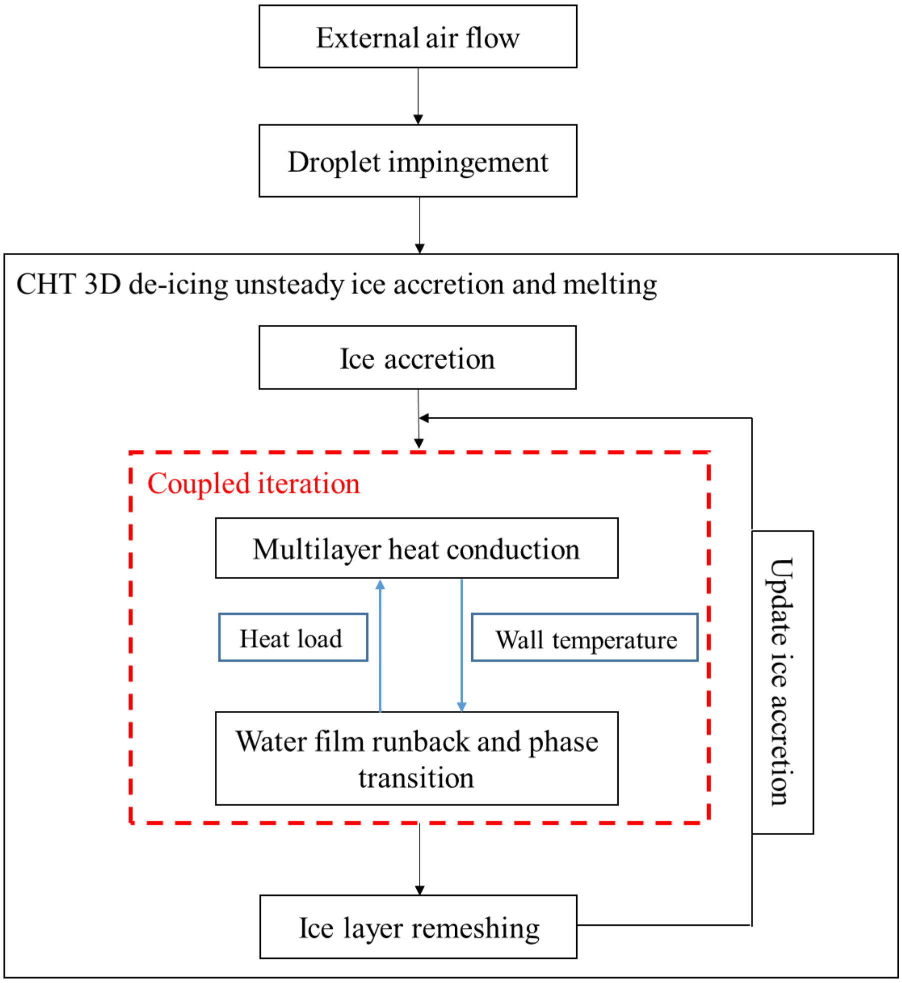
External air flow
Droplet impingement
CHT 3D de-icing unsteady ice accretion and melting
Ice accretion
Coupled iteration
Multilayer heat conduction
Heat load
Wall temperature
Water film runback and phase transition
Update ice accretion
Ice layer remeshing

Fig. 3.

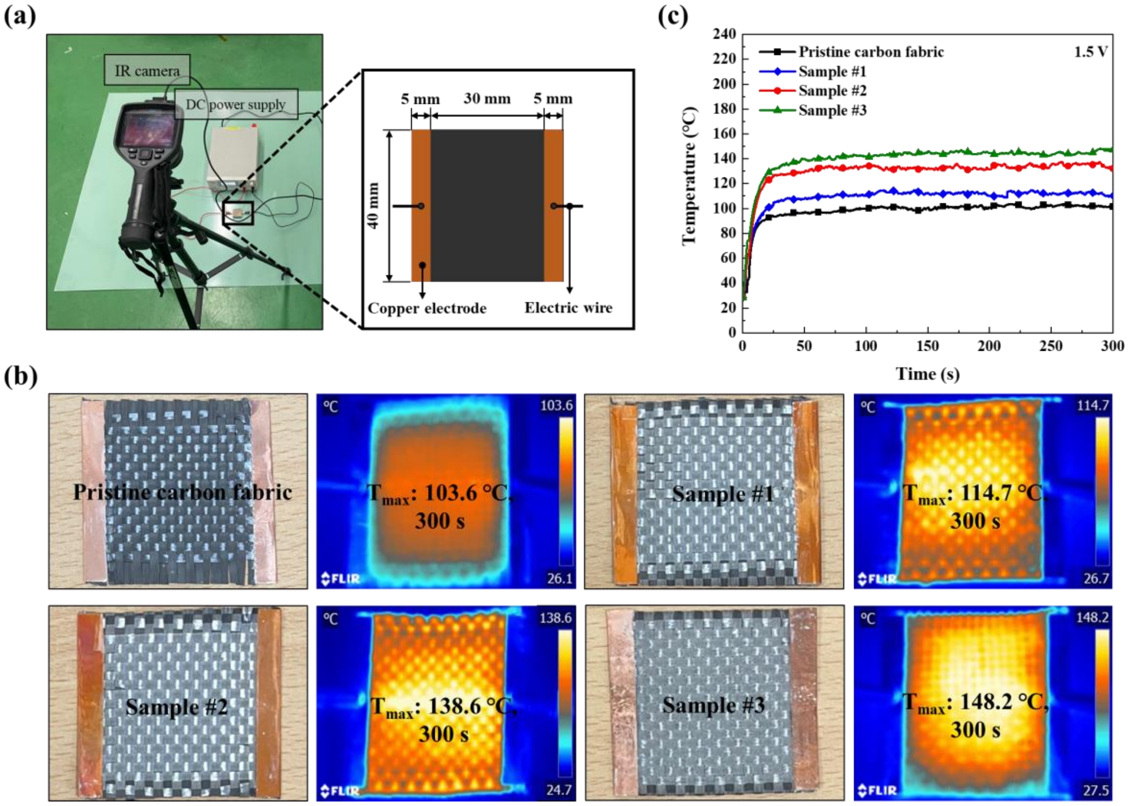
(a)
IR camera
DC power supply
5 mm
30 mm
5 mm
40 mm
Copper electrode
Electric wire
(c)
Pristine carbon fabric
Sample #1
Sample #2
Sample #3
1.5 V
Temperature (°C)
0
20
40
60
80
100
120
140
160
180
200
220
240
Time (s)
0
50
100
150
200
250
300
(b)
Pristine carbon fabric
°C
103.6
T_max: 103.6 °C,
300 s
26.1
FLIR
Sample #1
°C
114.7
T_max: 114.7 °C,
300 s
26.7
FLIR
Sample #2
°C
138.6
T_max: 138.6 °C,
300 s
24.7
FLIR
Sample #3
°C
148.2
T_max: 148.2 °C,
300 s
27.5
FLIR

Fig. 4.

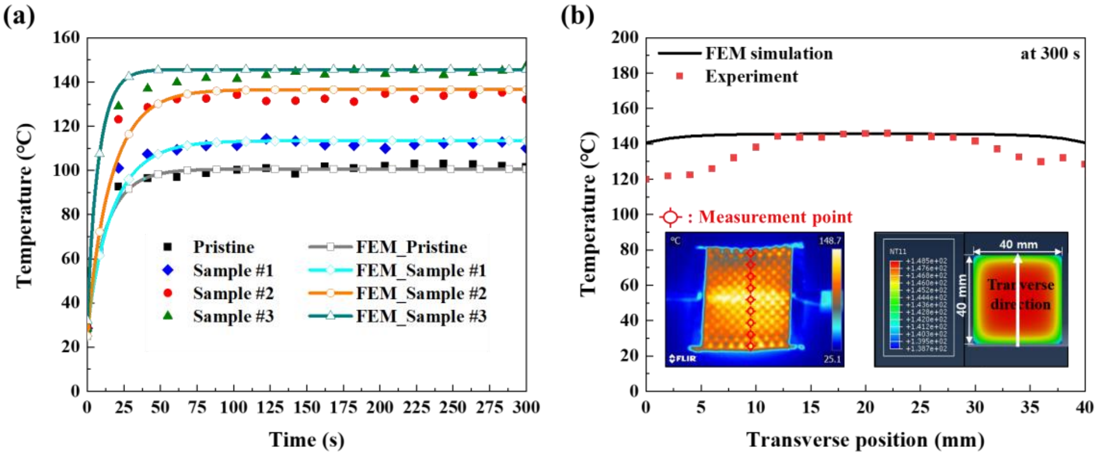
(a)
Temperature (°C)
160
140
120
100
80
60
40
20
0
0
25
50
75
100
125
150
175
200
225
250
275
300
Time (s)
Pristine
Sample #1
Sample #2
Sample #3
FEM_Pristine
FEM_Sample #1
FEM_Sample #2
FEM_Sample #3
(b)
Temperature (°C)
200
180
160
140
120
100
80
60
40
20
0
0
5
10
15
20
25
30
35
40
Transverse position (mm)
FEM simulation
Experiment
at 300 s
: Measurement point
°C
148.7
25.1
FLIR
NT11
+1.485e+02
+1.476e+02
+1.468e+02
+1.460e+02
+1.452e+02
+1.444e+02
+1.436e+02
+1.428e+02
+1.420e+02
+1.412e+02
+1.403e+02
+1.395e+02
+1.387e+02
40 mm
40 mm
Transverse direction

Fig. 5.

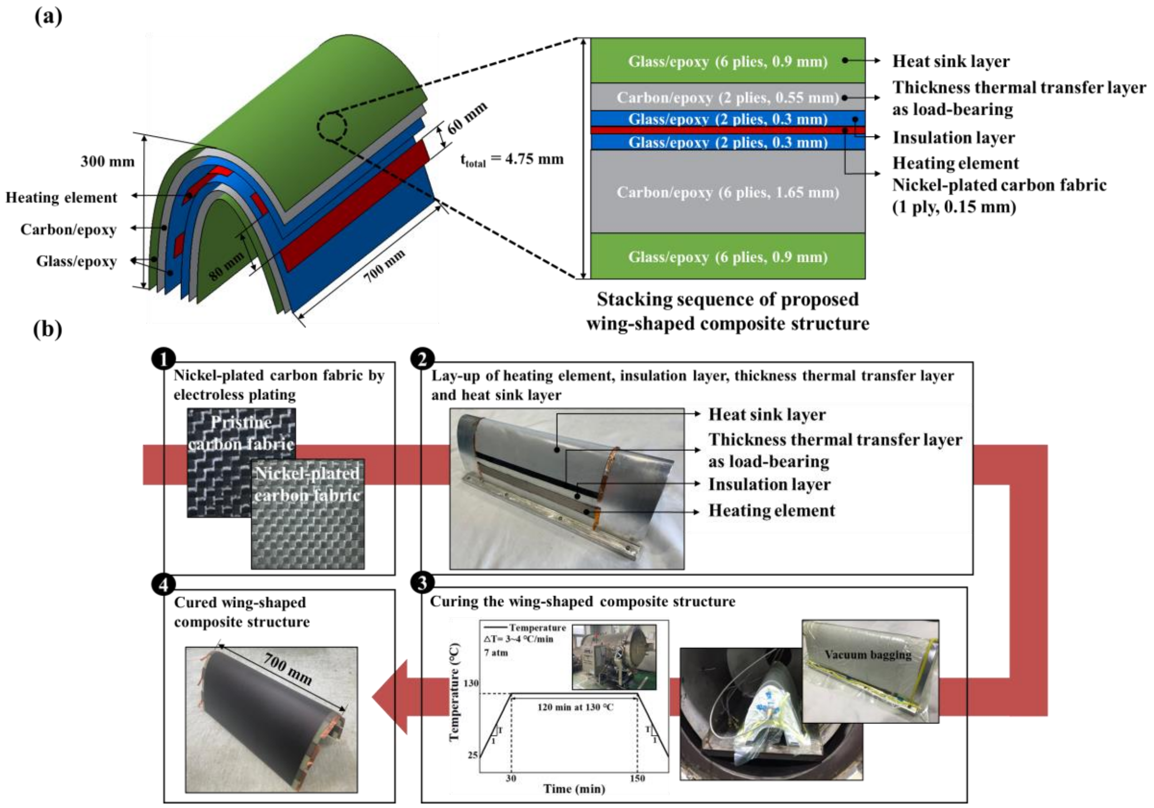
(a)
300 mm
Heating element
Carbon/epoxy
Glass/epoxy
80 mm
60 mm
700 mm
t_{total} = 4.75 mm
Glass/epoxy (6 plies, 0.9 mm)
Carbon/epoxy (2 plies, 0.55 mm)
Glass/epoxy (2 plies, 0.3 mm)
Glass/epoxy (2 plies, 0.3 mm)
Carbon/epoxy (6 plies, 1.65 mm)
Glass/epoxy (6 plies, 0.9 mm)
Heat sink layer
Thickness thermal transfer layer as load-bearing
Insulation layer
Heating element
Nickel-plated carbon fabric (1 ply, 0.15 mm)
Stacking sequence of proposed wing-shaped composite structure
(b)
❶
Nickel-plated carbon fabric by electroless plating
Pristine carbon fabric
Nickel-plated carbon fabric
❷
Lay-up of heating element, insulation layer, thickness thermal transfer layer and heat sink layer
Heat sink layer
Thickness thermal transfer layer as load-bearing
Insulation layer
Heating element
❸
Curing the wing-shaped composite structure
Temperature
ΔT= 3~4 °C/min
7 atm
Temperature (°C)
130
25
120 min at 130 °C
1
1
1
1
30
150
Time (min)
Vacuum bagging
❹
Cured wing-shaped composite structure
700 mm

Fig. 6.

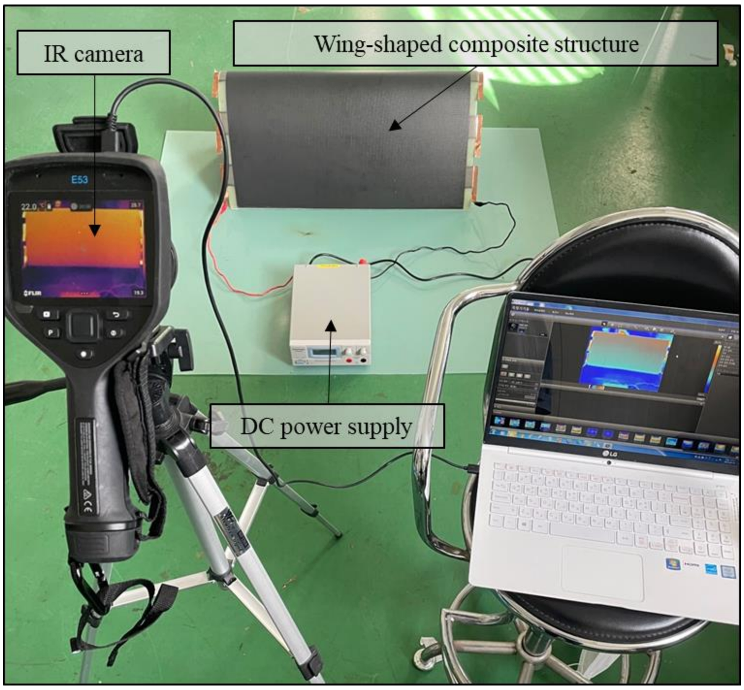

Fig. 7.

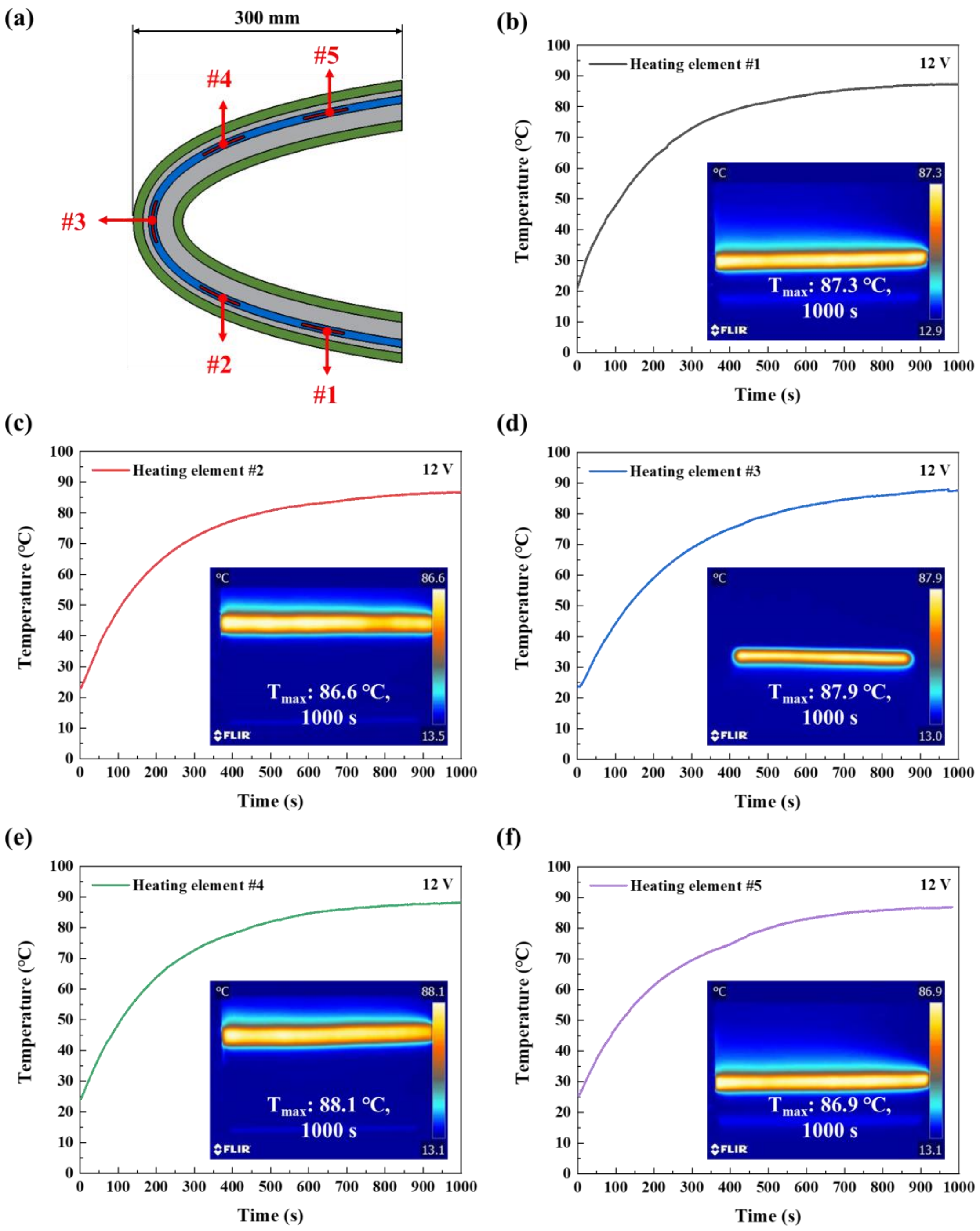
(a)
300 mm
#5
#4
#3
#2
#1
(b)
Heating element #1
12 V
Tmax: 87.3 °C, 1000 s
87.3
12.9
(c)
Heating element #2
12 V
Tmax: 86.6 °C, 1000 s
86.6
13.5
(d)
Heating element #3
12 V
Tmax: 87.9 °C, 1000 s
87.9
13.0
(e)
Heating element #4
12 V
Tmax: 88.1 °C, 1000 s
88.1
13.1
(f)
Heating element #5
12 V
Tmax: 86.9 °C, 1000 s
86.9
13.1
°C
FLIR
Temperature (°C)
Time (s)
0
10
20
30
40
50
60
70
80
90
100
0
100
200
300
400
500
600
700
800
900
1000

Fig. 8.

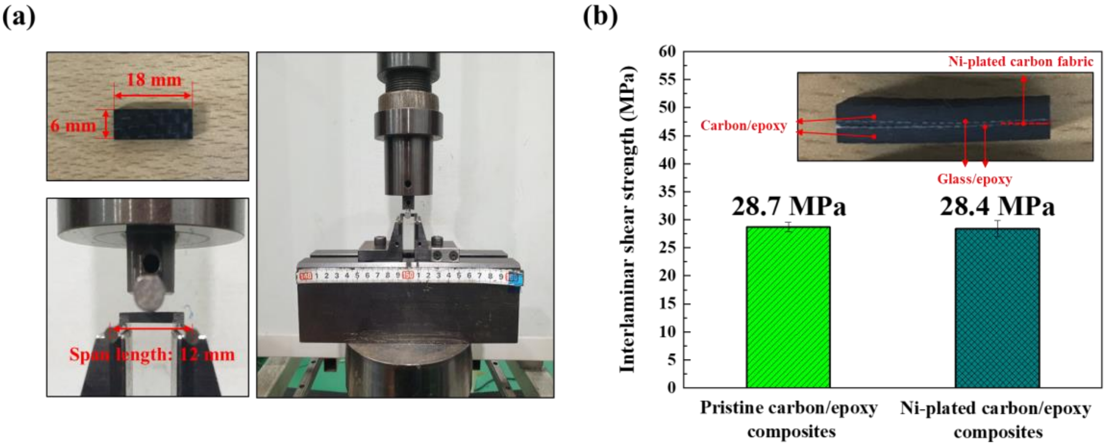
(a)
18 mm
6 mm
Span length: 12 mm
(b)
Interlaminar shear strength (MPa)
0
5
10
15
20
25
30
35
40
45
50
55
60
Ni-plated carbon fabric
Carbon/epoxy
Glass/epoxy
28.7 MPa
28.4 MPa
Pristine carbon/epoxy composites
Ni-plated carbon/epoxy composites

Fig. 9.

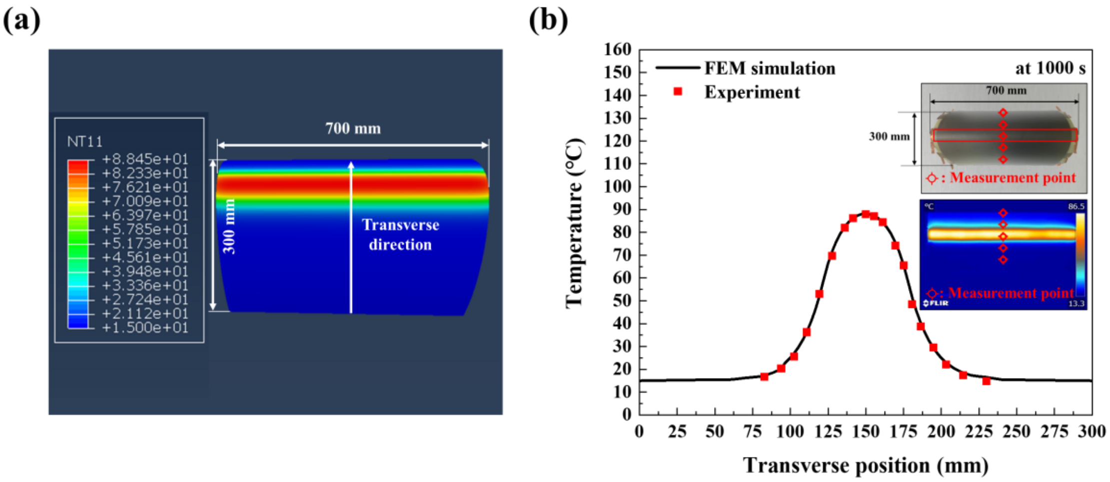
(a)
NT11
+8.845e+01
+8.233e+01
+7.621e+01
+7.009e+01
+6.397e+01
+5.785e+01
+5.173e+01
+4.561e+01
+3.948e+01
+3.336e+01
+2.724e+01
+2.112e+01
+1.500e+01
700 mm
300 mm
Transverse direction
(b)
FEM simulation
Experiment
at 1000 s
700 mm
300 mm
◇: Measurement point
86.5
13.3
◇: Measurement point
Temperature (°C)
Transverse position (mm)
0 10 20 30 40 50 60 70 80 90 100 110 120 130 140 150 160
0 25 50 75 100 125 150 175 200 225 250 275 300

Fig. 10.

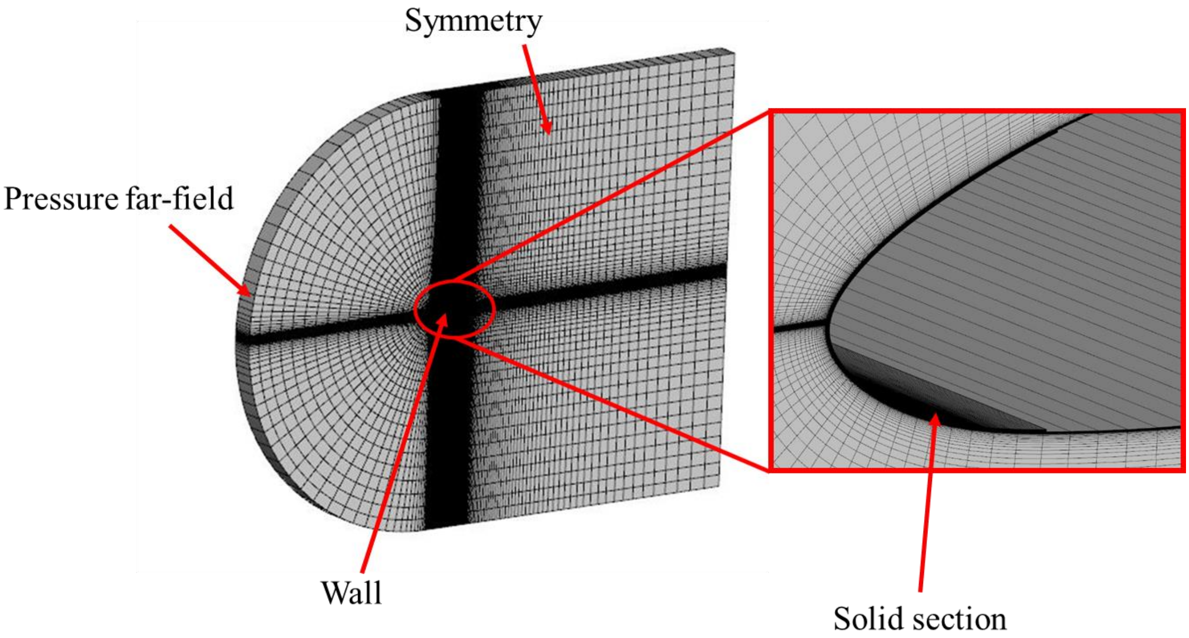

Fig. 11.

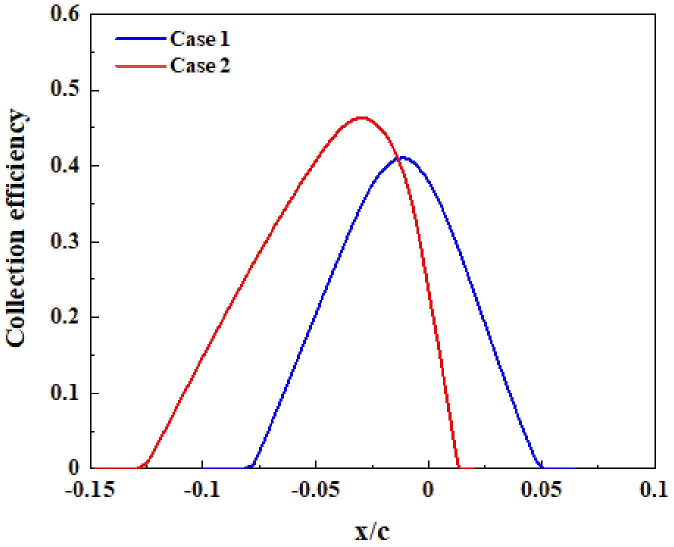
Case 1
Case 2
Collection efficiency
0.6
0.5
0.4
0.3
0.2
0.1
0
-0.15
-0.1
-0.05
0
0.05
0.1
x/c

Fig. 12.

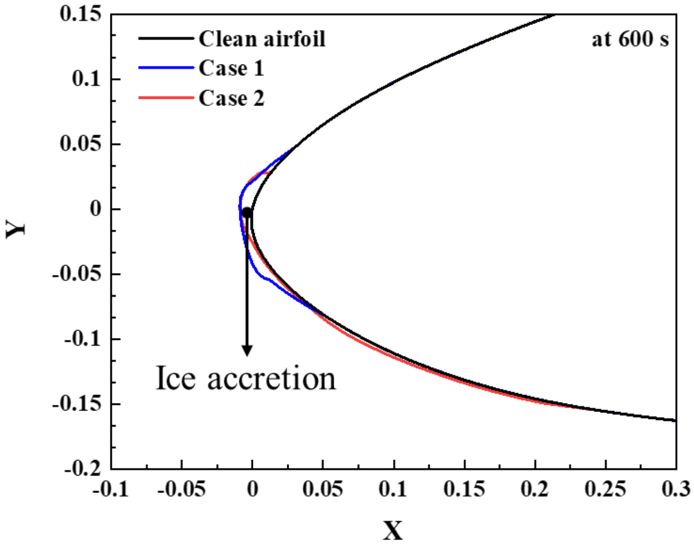

Clean airfoil
Case 1
Case 2
at 600 s
Ice accretion
Y
X
0.15
0.1
0.05
0
-0.05
-0.1
-0.15
-0.2
-0.1
-0.05
0
0.05
0.1
0.15
0.2
0.25
0.3

Fig. 13.

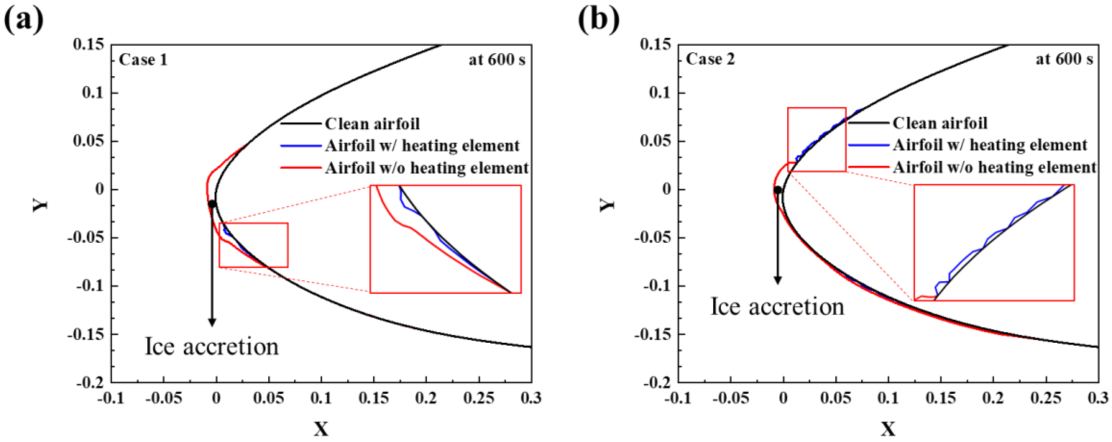

Fig. 14.

Table Captions

Table 1 Comparison between the electro-thermal heating elements reported in literature.

Table 2 Compositions of the pristine and nickel-plated carbon fabrics (samples #1, #2, and #3) obtained via energy-dispersive x-ray spectroscopy (EDS).

Table 3 Thermal and electrical properties of the pristine carbon fabric and samples #1, #2, and #3.

Table 4 The h_{r+c} values of the heating elements at an applied voltage of 1.5 V.

Table 5 Surface temperatures of the wing-shaped composite at an applied voltage of 12 V.

Table 6 Flight conditions for the multiphysics icing simulation.

Table 1

Study	Heating elements	ΔT_{max} (°C)	Power density (kW/m^2)	h_{r+c} (W/°C)
This study	Nickel-plated carbon fabric	128	4.04	0.054
Cao *et al.* [37]	Nickel-plated carbon fabric	36	0.60	0.026
Choi *et al.* [44]	Nickel-plated carbon fabric	110	31.70	0.091
Falzon *et al.* [24]	Carbon-based textile	35	1.20	1.540
Yao *et al.* [25]	Carbon-based textile	132	6.50	0.123
Yao *et al.* [28]	CNT dispersed film	40	1.14	0.120
Yoon *et al.* [29]	CNT dispersed film	115	6.40	0.034
Kim *et al.* [30]	CNT dispersed film	135	8.40	0.156
Tian *et al.* [31]	Carbon fabric + graphene coating	119	6.00	0.011
Sui *et al.* [32]	Graphene dispersed film	185	20.00	0.030
Vertuccio *et al.* [33]	Graphene dispersed film	110	4.12	0.094

Table 2

Sample	Weight percentage (wt. %) / Atomic percentage (at. %)		
	Ni	Cu	C
Pristine carbon fabric	0.00/0.00	0.00/0.00	100/100
Sample #1	58.22/39.82	29.31/18.52	12.46/41.66
Sample #2	68.82/50.40	21.37/14.46	9.81/35.14
Sample #3	86.43/97.04	8.80/1.87	4.77/1.10

Table 3

Material	Nickel plating thickness (μm)	Electrical resistance (Ω)	Electrical conductivity (S/m)	Thermal conductivity (W/m·K)	Specific heat capacity (J/K·kg)
Pristine carbon fabric	0.000	0.159	5.506×10^3	0.623	1.006
Sample #1	0.901	0.146	6.997×10^3	0.749	0.912
Sample #2	0.971	0.083	10.51×10^3	0.777	0.869
Sample #3	0.987	0.046	19.16×10^3	0.833	0.835

Table 4

Material	V_0 (V)	I_C (A)	T_0 (°C)	T_m (°C)	h_{r+c} (W/°C)
Pristine carbon fabric	1.5	3.21	28	103.6	0.064
Sample #1	1.5	3.58	28	114.7	0.062
Sample #2	1.5	4.05	28	138.6	0.055
Sample #3	1.5	4.31	28	148.2	0.054

Table 2

Heating element position	Voltage (V)	Current (A)	Power density (kW/m^2)	Maximum temperature, T_m (℃)
1	12	7.3	2.09	87.3
2	12	7.2	2.06	86.6
3	12	7.4	2.11	87.9
4	12	7.5	2.14	88.1
5	12	7.2	2.06	86.9

Table 6

Cases	Temperature (℃)	Velocity (m/s)	LWC (g/m^3)	MVD (μm)	AoA (°)
Case 1	-16	96.159	0.45	21.25	0
Case 2	-6	96.159	0.35	26.25	4